J Mol Model (2015) 21: 129
DOI 10.1007/s00894-015-2676-3

ORIGINAL PAPER

DFT study of zinc, cadmium, mercury, copper, silver, and gold complexes of 21,23-dioxaporphyrin and one-dimensional arrays of those complexes

Ulises Jiménez Castillo[1] · **Héctor López**[1] · **Patricia Guadarrama**[1] · **Serguei Fomine**[1]

Received: 10 November 2014 / Accepted: 7 April 2015 / Published online: 28 April 2015

Abstract Complexes of 21,23-dioxaporphyrin with neutral Zn, Cd, Hg, Cu, Ag, and Au atoms as well as some one-dimensional arrays of those complexes containing up to ten repeat units were modeled at the PBE/def2-TZVPP level of theory with D3 empirical dispersion correction. The binding energy between the metal atom and the macrocycle was found to vary from 90 kcal/mol for Cu to −14 kcal/mol for Hg. Strong charge transfer from the metal to the macrocycle accompanied complex formation. The complexes were able to form dimers and nanoarrays that were held together mostly by dispersion forces. Different types of dimers were studied: face-to-face (F) and two types of parallel-displaced ones. F dimers were calculated to be the lowest-energy structures for Cu and Ag systems. Nanoarray formation was studied for these complexes. The band gaps (E_g) of the nanoarrays were found to be smaller than 1 eV, and decreased slightly as the number of repeat units in the nanoaggregates increased. The ionization potentials and electron affinities were greatly affected by the number of repeat units due to the delocalization of polarons over the entire nanoarray. The polaron delocalization and the related reorganization energies depended to a considerable extent on the metal present in the complex. For the studied nanoarrays, the reorganization energies for hole and electron transport decreased linearly with $1/n$, where n is the number of repeat units in the nanoaggregate; for an infinitely long chain, the reorganization energy was zero for electron transport and 0.03–0.04 eV for hole transport.

✉ Serguei Fomine
fomine@servidor.unam.mx

[1] Instituto de Investigaciones en Materiales, Universidad Nacional Autónoma de México, Apartado Postal 70-360, CU, Coyoacán, Mexico, DF 04510, Mexico

Keywords Dioxaporphyrin · DFT · Dispersion correction · Reorganization energy · Polarons

Introduction

Porphyrins are multifunctional molecules that are mostly found as ligands in complexes where the nitrogen atoms in the porphyrin interact with a metal. Due to the redox properties of metals and the rigid planar aromatic structures of porphyrins, such metal–porphyrin combinations play important roles in oxygen and electron transfer, as well as in light-harvesting processes in metalloproteins [1–5].

Therefore, ever since the crystal structure of a porphyrin was solved for the first time [6], the number of papers describing chemical and physical properties of porphyrins has grown exponentially—especially papers relating to the development of new techniques for synthesizing porphyrins [7] and potential applications of porphyrins in solar cells [8–11], molecular recognition [12–14], catalysis [15], electrochemistry [16], sensors [17, 18], data storage [19], and optoelectronics [20–26]. Porphyrins are able to self-assemble both in solution and in the solid state, forming one-, two-, or three-dimensional structures due to coordination, hydrogen bonding, and π–π stacking. It has recently been demonstrated that submicrometer one-dimensional self-assembled porphyrin architectures can be obtained [27, 28]. Core modification of porphyrins through the introduction of various heteroatoms in place of the nitrogen atoms permits the preparation of a series of new heterocycles that may have interesting properties in terms of their binding abilities. Thus, a series of oxygen-containing porphyrins in which the extent of substitution was varied systematically have been prepared [29].

Porphyrin complexes with divalent cations are extremely stable neutral molecules where two pyrrolic nitrogens in the

porphyrin unit release their protons and bind a dication, forming a metalloporphyrin. It was shown in a recent paper [30] that metalloporphyrins are capable of forming one-dimensional nanoarrays. These nanoarrays have a relatively large band gap (about 2 eV) that does not depend on the size of the nanoarray, suggesting that there is little electronic coupling between the metal ions. The pyrrolic nitrogens in the porphyrin macrocycle have reduced affinities for neutral metal atoms compared to the anionic forms of those nitrogens present in metallated porphyrins. Core-modified porphyrins where an NH group is replaced by a heteroatom with a lone pair could be interesting systems for stabilizing neutral metal atoms. The formation of nanoarrays from metal complexes of hetero-core-modified porphyrins can be viewed as a way to stabilize a single-atom nanowire if the nanoarray is long enough and there is sufficient overlap between the orbitals of the metal atoms.

21,23-Dioxaporphyrins (DOP) are macrocycles in which two pyrrole nitrogens are replaced by furan oxygens (Fig. 1). Tetraphenyl-21,23-dioxaporphyrin is capable of forming complexes with $NiCl_2$ in which the Ni^{2+} can easily be reduced to Ni^{+}, suggesting that the macrocycle stabilizes low oxidation states of metal ions [31]. Organonickel complexes of 21,23-dioxaporphyrin have also been prepared in which the oxidation state of nickel is close to zero [32]. Therefore, 21,23-dioxaporphyrin is potentially capable of stabilizing neutral metal atoms too. However, to the best of our knowledge, there are neither the experimental nor the theoretical data required to prove or disprove this hypothesis. Therefore, we decided to explore the formation of complexes between 21,23-dioxaporphyrin and neutral metal atoms using quantum chemistry tools. We have also studied the formation and the electronic properties of one-dimensional nanoarrays of those complexes as possible models for stable single-atom nanowires.

It was shown recently that dispersion interactions dominate in fullerene/porphyrin and porphyrin/porphyrin complexes and in nanoarrays [30, 33]. Therefore, these dispersion interactions must be taken into account when modeling porphyrin complexes. For large systems involving multiple fragments bound together mostly by dispersion forces, wavefunction-based methods are prohibitively expensive, so DFT with explicit or implicit dispersion correction is the method of choice.

Computational details

All geometry optimizations and energy calculations were carried out using the PBE [34, 35] functional and the def2-TZVPP basis set with the resolution of identity and the multipole accelerated resolution of identity approximations as implemented in the TURBOMOLE 6.6 code [36]. The D3 empirical dispersion correction was used for all optimizations [37]. No symmetry restrictions were imposed during the optimizations. Restricted and unrestricted DFT were used for closed- and open-shell systems, respectively. The use of such a large basis set allowed us to significantly decrease the basis set superposition error in the binding-energy calculations, making counterpoise correction unnecessary. 21,23-Dioxaporphyrin nanoarrays are denoted "*n*DOP-M" in this work, where *n* is the number of 21,23-dioxaporphyrin units in the nanoarray and M is a metal atom. The additional presence of a plus or minus symbol as a suffix indicates a cation or an anion radical, respectively. Frequency calculations were performed for dimers and nanoarrays to ensure that an energy minimum had been located. Moreover, all restricted closed-shell solutions for all dimers and nanoarrays were tested for triplet instability to ensure that the closed-shell singlet state was the ground state for these systems.

Although neither experimental nor theoretical data on the stacking energies of 21,23-dioxaporphyrin are available, a method similar to that used in this manuscript—only with a smaller basis set (def2-SVP)—has been used to reproduce the interaction energy of the C_{60}/tetraphenylporphyrin complex estimated at the scaled opposite spin second-order Møller–Plesset (SOS-MP2) level of theory extrapolated to the basis set limit (27.0 vs. 31.5 kcal/mol) [38]. Both the C_{60}/tetraphenylporphyrin and the 21,23-dioxaporphyrin complexes show large contributions of dispersion interactions to the total interaction energy, so we believed that the method used in this study would perform reasonably well.

Results and discussion

Monomers

Figure 1 and Table 1 show the optimized structures and properties of DOP-Zn, DOP-Cu, DOP-Cd, DOP-Ag, DOP-Hg, and DOP-Au complexes. As seen in Table 1, most of the metal atoms form strong complexes with the DOP macrocycle. The highest binding energy is seen for the Cu atom (90 kcal/mol), while the lowest is observed for the Hg complex; according to the calculations, this complex is unstable, with a negative binding energy of −14 kcal/mol. The binding energies for metals of group Ib are notably higher than those for group IIb, and in both cases the energies decrease with atomic radius. According to Table 1, the dispersion contributions to the binding energy are relatively small, representing 10–30 % of the total binding energy. The most important contribution to the binding comes from the DFT term. Inspection of the optimized geometries of the DOP-M complexes reveals that the metal atom interacts mostly with the nitrogens of the macrocycles, not with the oxygens, as seen from the shorter M–N distances than M–O distances. In all of the complexes, the central metal atom has a significant positive charge;

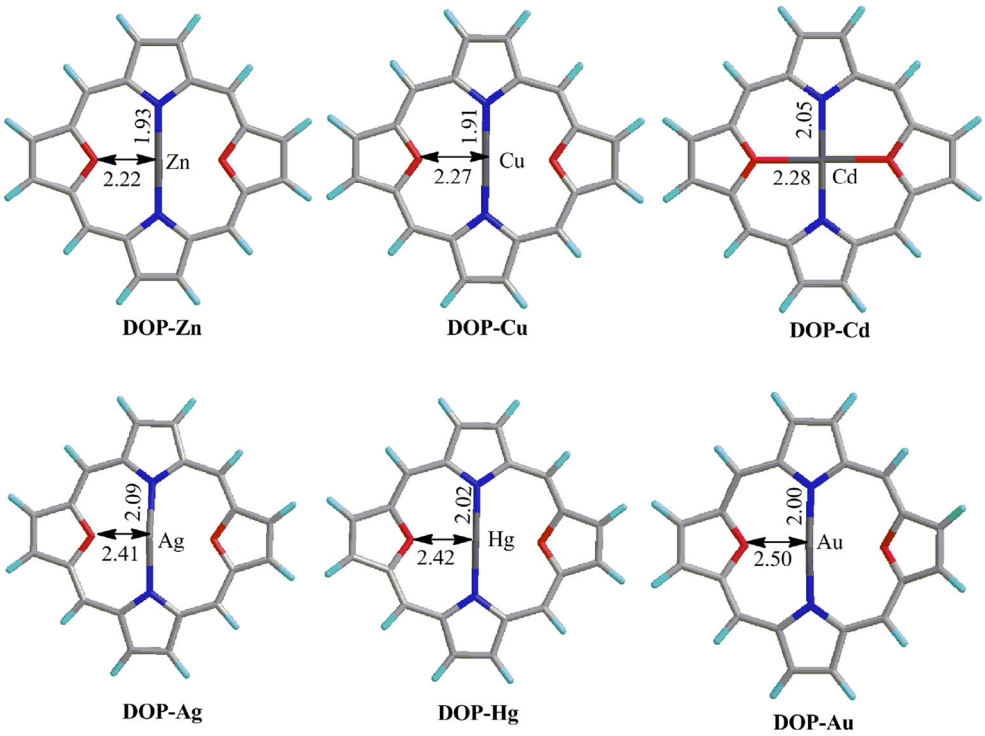

Fig. 1 Optimized geometries of 21,23-dioxaporphyrin complexes with metals, and selected distances within the complexes (Å)

Table 1 shows that these charges range from +1.57 for DOP-Zn to +0.59 for DOP-Au. The natural charge at the metal atom correlates with the Pauling electronegativity within each subgroup. Natural population analysis reveals that the positive charge at the metal atom is a result of electron transfer from the valence *s* shell of the metal to the macrocycle. Cu, Ag, and Au have one electron in this shell, while Zn, Cd, and Hg have two electrons. This is why the natural charges on the Zn, Cd, and Hg atoms are roughly 1 electron higher than those on Cu, Ag, and Au. The lower first ionization potentials of Cu, Ag and Au as compared to Zn, Cd, and Hg result in higher binding energies for the former.

The drop in the interaction energy within each subgroup (Ib and IIb) is related to the increasing radius of the metal atom. This is also reflected in the N–M–N and O–M–O angles of the DOP-M complexes, which show the shift of the metal atom away from the macrocycle plane. Large atoms do not fit into the macrocycle cavity, thus decreasing the interaction between the metal and the nitrogen atoms.

Table 1 DFT (E_{dft}) and dispersion (E_{disp}) contributions to the total binding energy (E_{tot}, kcal/mol); the angles N–M–N and O–M–O (degrees); the natural charges (Q) (electrons) on the metal atoms in DOP-M complexes; and the Pauling electronegativity (EN) values for the metal atoms

Complex	N–M–N	O–M–O	E_{dft}	E_{disp}	E_{tot}	Q	EN
DOP-Cu	180.0	180.0	85.0	5.8	90.8	0.83	1.90
DOP-Zn	179.8	179.7	49.9	5.6	55.5	1.57	1.65
DOP-Ag	152.5	138.5	43.2	6.7	49.9	0.74	1.93
DOP-Cd	172.5	166.8	14.6	6.5	21.1	1.53	1.69
DOP-Au	165.3	144.5	44.9	7.3	52.3	0.59	2.54
DOP-Hg	168.6	151.4	-20.6	6.5	−14.0	1.33	2.00

Dimers

Since DOP-Hg was found to be unstable, it was dropped from the rest of the study. The formation of dimers was studied for all the other systems. Figure 2 shows the optimized geometries of the dimers, and their properties are listed in Table 2. Different types of dimers were detected. Face-to-face (F) and parallel-displaced dimers (PD) were found for all systems. For the DOP-Zn and DOP-Cd macrocycles, two types of PD dimers were found: PD1, where the metal atom interacts with methyne carbons of the neighboring macrocycle, and PD2, where the metal atom interacts with nitrogen atoms of the adjacent macrocycle (Fig. 2). For the systems containing Cu, Ag, and Au, only two type of dimers were detected: F and PD. In this case, the configuration of the PD dimer was similar to that of 2DOP-Zn-PD2 and 2DOP-Cd-PD2, where the metal atom interacts with nitrogens of the neighboring macrocycle. The binding energies of the dimers as well as the contributions of the dispersion energies to the total binding energies are listed in Table 2. As seen, all of the dimers are rather stable, with binding energies ranging from 23 to 33 kcal/mol. It is noteworthy that, unlike the binding between the metal atom and the macrocycle, where the contribution from dispersion interactions is quite small, the binding interactions in dimers

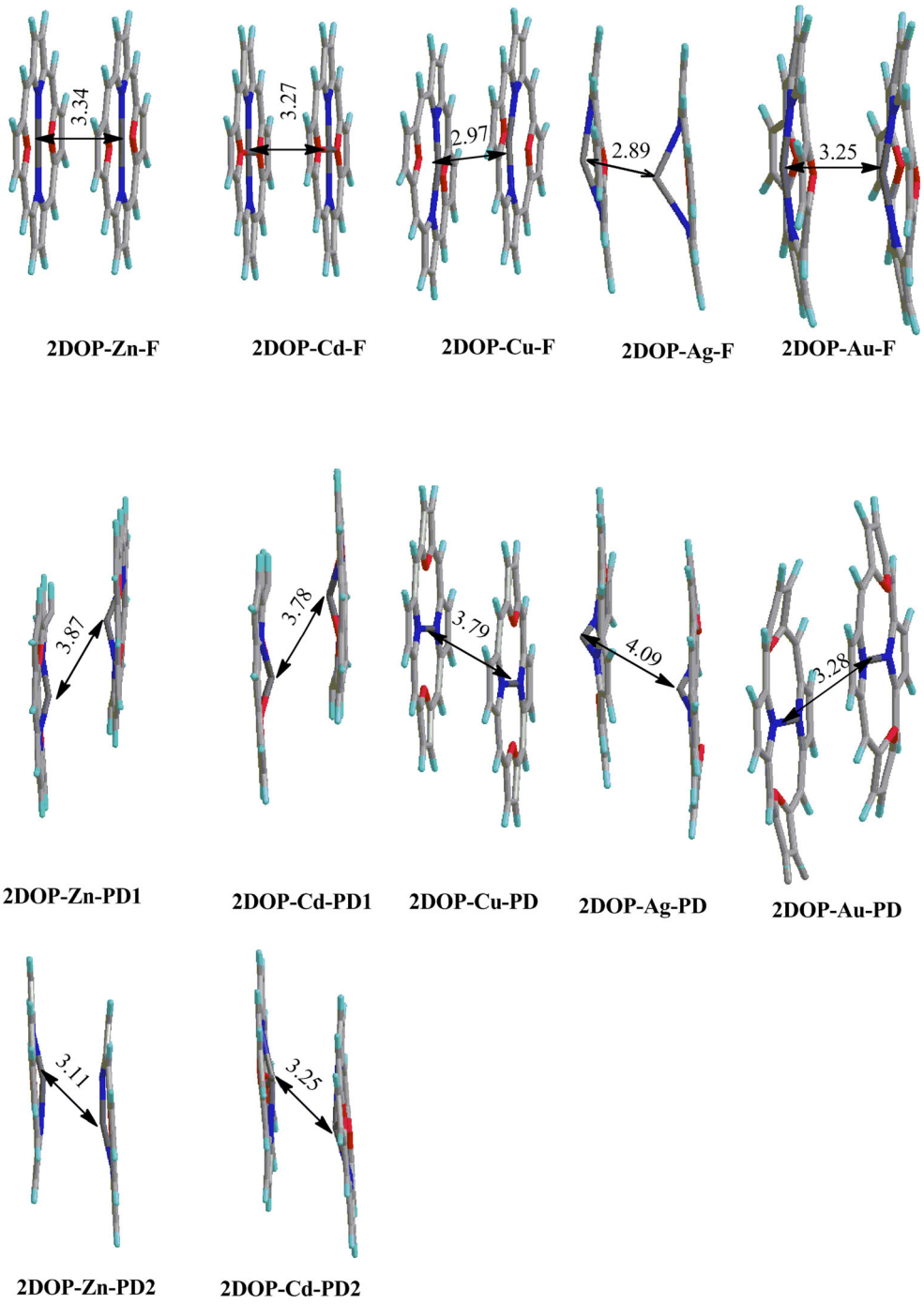

Fig. 2 Optimized geometries of dimers and the corresponding metal–metal distances (Å)

between macrocycles are mostly due to dispersion interactions. Moreover, for some of the dimers (Table 2), the binding energies are negative at the pure DFT level. This observation is similar to that noted for metalloporphyrin dimers and porphyrin–C60 complexes, in which dispersion interactions also dominate [30, 33]. The relative stability of the studied dimer depends on the metal present (Table 2). Thus, for Zn and Cd, the PD1 dimers are the most stable, whereas for Cu and Ag, the F dimers are the lowest-energy structures. In the case of Au, the most stable dimer is PD. As seen in Table 2, the relative stabilities of the dimers range from 1 to 8 kcal/mol. It is noteworthy that the stability calculations performed for dimers of open-shell complexes (DOP-Cu, DOP-Ag, and DOP-Au) showed that, in all cases, the restricted closed-shell singlet solution was stable. The stability of the closed solution means that, for F complexes, there is a significant overlap in electronic density between metal atoms, and those dimers are promising building blocks for nanoaggregates in which there is direct interaction between all metal atoms of nanoaggregates.

Table 2 DFT (E_{pbe}) and dispersion (E_{disp}) contributions to the total binding energy (E_{tot}) as well as the relative total energy (E_{rel}) of each dimer (kcal/mol)

Dimer	E_{pbe}	E_{disp}	E_{tot}	E_{rel}
2DOP-Cu-F	−1.2	28.1	26.9	0
2DOP-Cu-PD	−1.5	26.5	25.0	1.9
2DOP-Zn-F	−0.2	28.3	28.1	1.4
2DOP-Zn-PD1	4.5	25.0	29.5	0
2DOP-Zn-PD2	−5.3	29.6	24.3	5.2
2DOP-Ag-F	2.4	27.9	30.3	0
2DOP-Ag-PD	−2.6	25.6	23.0	7.3
2DOP-Cd-F	−1.1	28.8	27.7	5.5
2DOP-Cd-PD1	14.3	18.9	33.2	0
2DOP-Cd-PD2	−0.5	26.0	25.5	7.7
2DOP-Au-F	−1.5	26.8	25.3	1.8
2DOP-Au-PD	−1.3	28.4	27.1	0

Nanoaggregates formed by DOP-Cu and DOP-Ag

Since F dimers are the most stable ones for DOP-Cu and DOP-Ag metallocycles, they were selected as the nanoaggregate building blocks in the present work. Thus, tetramers, hexamers, octamers, and decamers of these metallocycles were studied, along with dimers. The optimized geometries of these nanoaggregates are shown in Fig. 3, and their properties are listed in Table 3.

As seen in Fig. 3, there are notable differences between the Cu- and Ag-containing nanoaggregates. This difference originates from the larger atomic radius of Ag than Cu. The Cu atom is small enough to fit within the cavity of the macrocycle (i.e., it is in the plane of the macrocycle) in *n*DOP-Cu nanoaggregates, while the Ag atoms in *n*DOP-Ag nanoaggregates reside between macrocycle planes (because the Ag atom does not fit in the macrocycle cavity), resulting in decreased regularity of the nanoaggregates in the latter case. Cu–Cu distances alternate in *n*DOP-Cu, revealing that *n*DOP-Cu nanoaggregates are formed by the interactions of dimers, although the shortest Cu–Cu distance in any *n*DOP–Cu nanoaggregate (3.08 Å) is somewhat larger than that in the dimer (2.97 Å). The difference between the largest and the shortest Cu–Cu distance tends to decrease in the central region of the nanoaggregate. The out-of-plane positions of the Ag atoms in *n*DOP-Ag nanoaggregates and the mismatch between the Ag–Ag and macrocycle–macrocycle equilibrium distances result in irregular Ag–Ag distances in *n*DOP-Ag nanoaggregates. The Ag–Ag distance consistently increases from the left to the right side of the nanoaggregate (as shown in Fig. 3), from 2.84 to 3.63 Å. This phenomenon is reflected in the electronic properties of the nanoaggregate. As seen from the Table 3, the binding energies per bond are higher for *n*-DOP-Ag, 34–35 kcal/mol, than for nanoaggregates of the *n*DOP-Cu series (25 kcal/mol). For all of the nanoaggregates, the largest contribution to the binding comes from dispersion, as also noted for the dimers. Moreover, the pure DFT energy is repulsive in all nanoaggregates of the *n*DOP-Cu series, while it is attractive for Ag-containing nanoaggregates (although it does not exceed 15 % of the total binding energy).

The band gaps (E_g) of the nanoaggregates were estimated by two different methods. The first method is simply the difference between the energies of the HOMO and LUMO, as obtained from a B3LYP/TZVPP single-point energy evaluation. The B3LYP HOMO–LUMO energy difference is a good approximation of E_g for conjugated organic polymers [39]. For nanoaggregates of the *n*DOP-Cu series, E_g monotonically decreases with nanoaggregate size, allowing us to linearly extrapolate E_g vs. $1/n$ to an infinitely long nanoaggregate, which yields 0.62 eV. This value is much smaller than the E_g values estimated for metalloporphyrin nanoaggregates containing Zn, Cd, or Hg dications [30]. There is no such clear trend in E_g for *n*DOP-Ag nanoaggregates due to their more irregular structures. However, E_g barely changes as the nanoaggregate length increases beyond 6DOP-Ag, as seen in Table 3. Therefore, the E_g values of infinitely long *n*DOP-Ag nanoaggregates probably lie somewhere between 0.4 and 0.6 eV according to B3LYP HOMO–LUMO energy estimation. However, this method has a serious drawback for these systems: B3LYP closed-shell solutions show triplet instability for all nanoaggregates, making such an approach unreliable in this case. As an alternative, we estimated the lowest excitation energies for all nanoaggregates using a time-dependent implementation of the CAM-B3LYP functional [40]. This method delivers reliable data for excitation energies even when there is only minor spatial overlap between the occupied and virtual orbitals involved in the excitations. This is the case for the excitations in metalloporphyrin nanoarrays, for which GGA functionals strongly underestimate the excitation energies [30]. Similar to the B3LYP functional, CAM-B3LYP shows triplet instability of the ground state. Therefore, the Tamm–Dancoff approximation (TDA) [41] was used to calculate the lowest excitation energies of the nanoaggregates, since it has been demonstrated that TDA reduces errors associated with triplet instability [42]. The stable broken-symmetry solution was used as the reference state. As seen in Table 3, the band gap is smaller than 1 eV for all nanoaggregates, showing a slight tendency to decrease with nanoaggregate size. There was no clear linear correlation between $1/n$ and E_g for both *n*DOP-Cu and *n*DOP-Ag systems, with Ag-containing nanoaggregates possessing slightly smaller band gaps than the corresponding Cu-containing systems. For *n*DOP-Cu nanoaggregates, the band gap tended to saturate for octamers and decamers, allowing us to estimate the band gap for an infinitely long chain as 0.5 eV. The irregular geometry of *n*-DOP-Ag nanoaggregates did not allow us to extrapolate E_g to an infinitely long chain. Nevertheless, as seen in Table 3, E_g

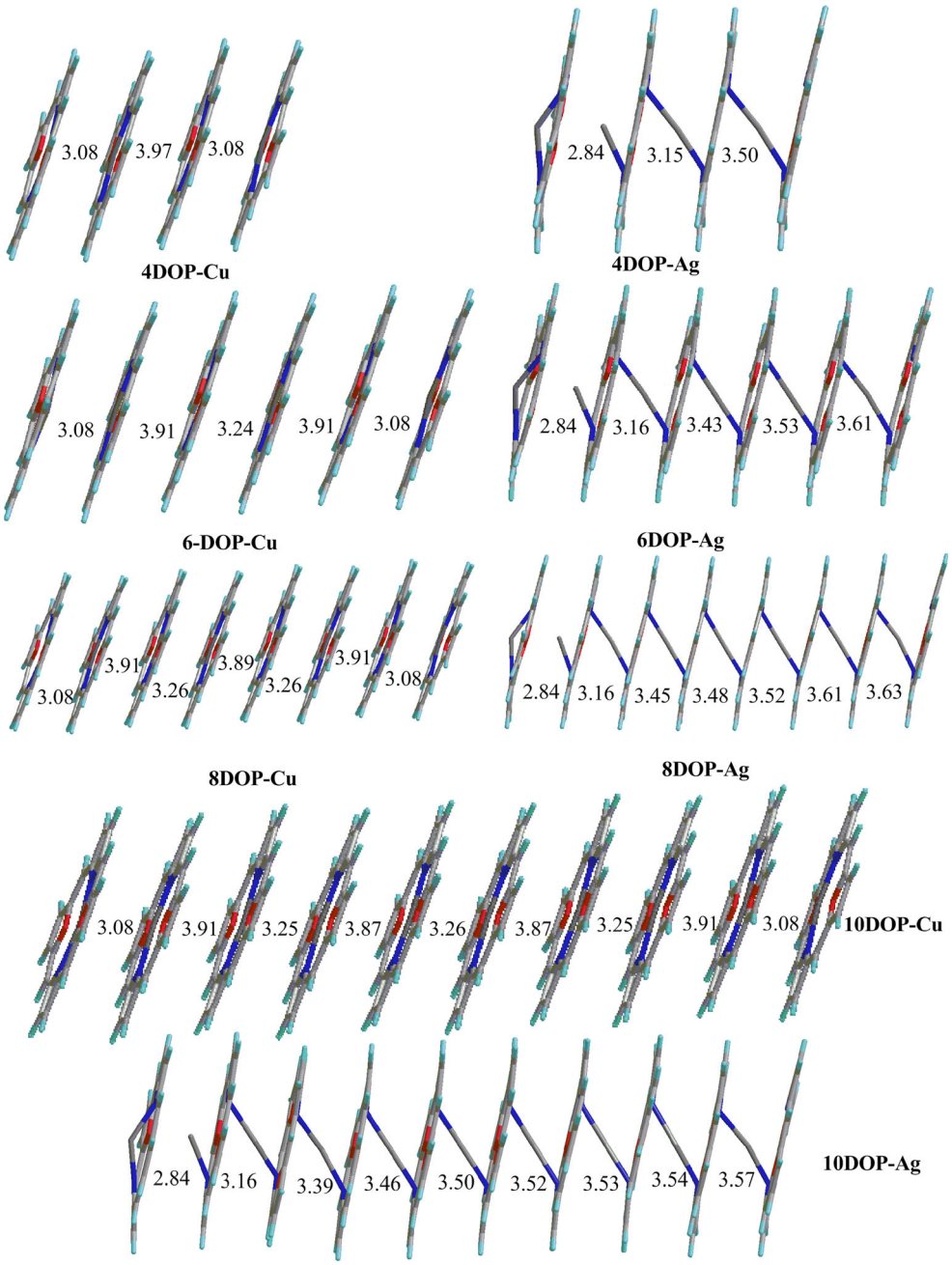

Fig. 3 Optimized geometries of Cu- and Ag-containing nanoarrays, along with the corresponding metal–metal distances (Å)

for an infinitely long Ag-containing nanoaggregate lies in the range 0.3–0.5 eV. The results from using both methods (the HOMO–LUMO B3LYP energy difference and the TDA-CAM-B3LYP excitation energy) are in reasonable agreement with one another, predicting E_g values of <1 eV for all nanoaggregates.

As seen in Table 3, the ionization potentials (IPs) and the electron affinities (EAs) of the nanoaggregates are markedly dependent on n, suggesting that both positive charge and negative charge are delocalized over the entire nanoaggregate. Thus, the 10DOP-Cu and 10DOP-Ag nanoarrays have IPs of close to 3.8 eV, which is significantly lower than the IP values of nanoarrays of Zn^{2+}-, Cd^{2+}-, and Hg^{2+}-containing metalloporphyrins (5 eV) [30], while the extrapolated IPs for infinitely long chains are 0.2–0.3 eV lower still. The EA increases with n for these nanoaggregates, reaching 2.3–2.4 eV for the infinitely long chains, which are slightly lower values than those estimated for metalloporphyrin nanoarrays. This difference may be related to the fact that metalloporphyrins contain metal dications whereas dioxaporphyrins have neutral metal atoms: this leads to lower IPs and EAs.

Figures 4 and 5 show polaron delocalization in cation and anion radicals of nanoarrays, respectively. In a polaron, the charge is associated with an unpaired electron, so polaron

Table 3 Total binding energies (E_{tot}) calculated using the PBE+D3 model, and the corresponding contributions from dispersion (E_{disp}) and DFT (E_{dft}, kcal/mol). The lowest excitation energies of the studied nanoaggregates were calculated with the TDA-CAM-B3LYP method (E_{gTDA}). Adiabatic ionization potentials (IP_a), electron affinities (EA_a), and reorganization energies for hole (λ_+) and electron (λ_-) transport (eV) are also shown

Complex	IP_a	EA_a	λ_+	λ_-	E_g	E_{gTDA}	E_{disp}	E_{dft}	E_{tot}
DOP-Cu	5.14	1.61	0.15	0.15	–	–	–	–	–
2DOP-Cu	4.81	1.83	0.13	0.28	1.09	0.60	–	–	–
4DOP-Cu	4.29	1.98	0.10	0.20	0.97	0.53	27.8	−2.3	25.5
6DOP-Cu	4.02	2.07	0.08	0.15	0.86	0.55	27.7	−2.5	25.2
8DOP-Cu	3.84	2.14	0.08	0.14	0.79	0.52	27.8	−2.8	25.0
10DOP-Cu	3.77	2.19	0.04	0.11	0.76	0.53	27.8	−2.9	24.9
∞DOP-Cu	3.52	2.38	0.03	0[a]	0.62	–	–	–	–
DOP-Ag	5.20	1.74	0.19	0.19	–	–	–	–	–
2DOP-Ag	4.86	1.89	0.14	0.26	1.10	0.57	–	–	–
4DOP-Ag	4.21	2.13	0.08	0.04	0.60	0.43	30.2	2.4	32.6
6DOP-Ag	4.01	2.16	0.09	0.06	0.49	0.36	29.9	4.4	34.2
8DOP-Ag	3.85	2.24	0.08	0.07	0.44	0.36	29.6	5.1	34.7
10DOP-Ag	3.78	2.29	0.06	0.05	0.54	0.47	30.2	5.3	35.5
∞DOP-Cu	3.40	2.45	0.04	0	–	–	–	–	–

[a] Extrapolated for 13-mer

delocalization can be visualized as unpaired electron density. As seen in Figs. 4 and 5, the delocalization patterns of polarons in nanoarrays depend on both the metal present and the nanoarray length. Thus, in *n*DOP-Cu+, the Cu *d* orbitals are involved in polaron delocalization, whereas they are not in *n*DOP-Ag+. This is due to the much stronger interaction of Cu than Ag with the macrocycle, allowing better orbital overlap. Moreover, the polaron cation in 10DOP-Cu+, the largest of the nanoarrays studied here, is uniformly delocalized over the d_z^2 orbitals of the Cu atoms and, to a much smaller extent, the *p* orbitals of N and O. For smaller nanoarrays, the delocalization of polaron cations in *n*DOP-Cu+is different. In smaller nanoaggregates, the polaron cation is delocalized over π orbitals of the macrocycle, *p* orbitals of the oxygen atoms, and, to some extent, *d* orbitals of the Cu atoms. This sudden change in the polaron cation delocalization pattern when the nanoarray size increases from 8 to 10 units may be related to the formation of a metal nanowire that is long enough to stabilize a positive charge better than the columnar structure of a macrocycle can. To support this hypothesis, we estimated the vertical IPs for two sets of systems. The first set comprised *n*DOP-Cu systems with the Cu atoms removed and the second set consisted of the same systems with the DOP macrocycles removed. This made it possible to monitor the effect of increasing the nanoarray length on the electronic properties of the DOP and Cu components separately. The results show that, in both cases, the IP decreases with nanoarray length, but it decreases faster for the Cu component. Thus, from 4DOP-Cu to 10DOP-Cu, the ionization energy of the *n*DOP system decreases by 0.60 eV, while that for the Cu component drops by 0.90 eV. This observation could explain why the polaron cation in 10DOP-Cu+ is mostly delocalized over the Cu atoms.

Unlike *n*DOP-Cu+, *n*DOP-Ag+ nanoaggregate polaron cations show irregular delocalization patterns due to the irregular distances between metal atoms. Similar to the Cu-containing nanoaggregates 2DOP-Cu+ to 8DOP-Cu+, the polaron cation is delocalized over the π orbitals of the macrocycle and *p* orbitals of oxygen atoms. Ag orbitals barely participate in polaron-cation delocalization.

The delocalization patterns of the anion polarons in *n*DOP-Cu− and *n*DOP-Ag− differ from those derived for polaron cations (Figs. 4 and 5): the polaron anions are delocalized over the *p* orbitals of nitrogen atoms and π orbitals of DOP units. Again, the participation of the metal atoms is more noticeable for the Cu-containing nanoaggregates than for the Ag-containing ones due to the stronger interaction of the Cu atoms with the DOP macrocycles. Similar to what was calculated for the polaron cations, the delocalization patterns of the polaron anions in *n*DOP-Ag− were found to be irregular due to the irregular macrocycle–macrocycle distances. On the other hand, the *n*DOP-Cu− nanoaggregates demonstrated more regular polaron-anion delocalization patterns. The polaron anion was delocalized uniformly across all the macrocycles and Cu atoms in the dimer and tetramer.

The key to understanding the conductivity of the nanoaggregates is to characterize the structural factors that influence their charge-transfer rates. It has been demonstrated that the solid-state hole mobility in arylamines is related to the internal reorganization energy (λ) [43–45]. The reorganization energy for hole mobility (λ_+) can be estimated as follows, so long as local vibronic coupling is dominant:

$$\lambda_+ = (E_n{}^+ - E_n) + (E_+{}^n - E_+).$$

Here, E_n and E_+ are the energies of the neutral and cationic species in their lowest-energy geometries, respectively, while $E_n{}^+$ and $E_+{}^n$ are the energies of the neutral and cationic species with the geometries of the cationic and neutral species, respectively. The reorganization energy for electron transport is defined similarly:

$$\lambda_- = (E_n{}^- - E_n) + (E_-{}^n - E_-).$$

In this case, E_n and E_- are the energies of the neutral and anionic species in their lowest-energy geometries, respectively, while $E_n{}^-$ and $E_-{}^n$ are the energies of the neutral and anionic species with the geometries of the anionic and the neutral species, correspondingly. Table 2 shows the calculated values of λ_+ and λ_- for the nanoaggregates. The reorganization energies for the nanoaggregates decrease with *n*. There are linear correlations between λ and 1/*n* with linear regression correlation coefficients (R^2) of 0.97 and 0.96 for hole and electron

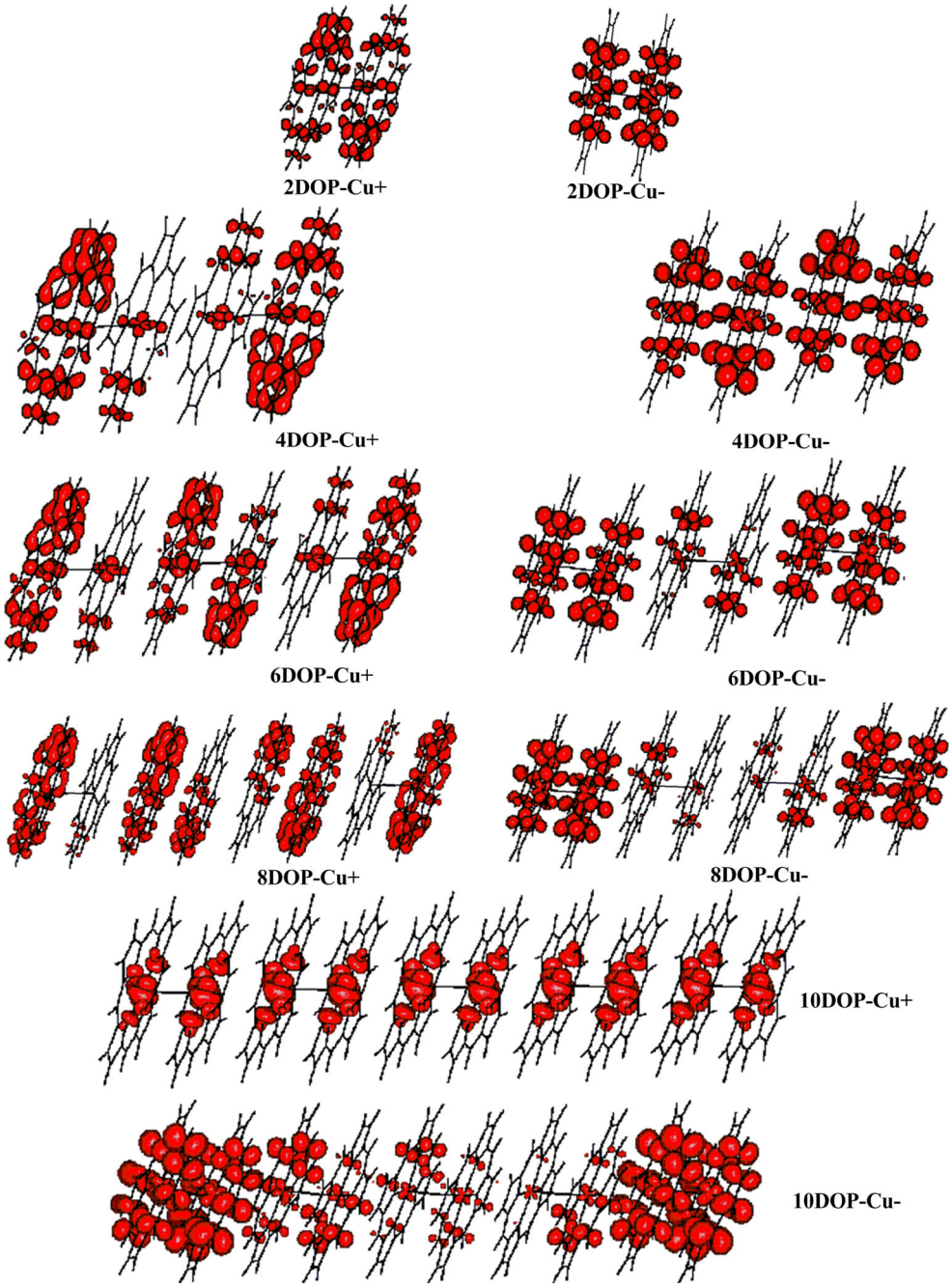

Fig. 4 Unpaired spin-density delocalization in cation and anion radicals of Cu-containing nanoarrays. (Isovalue=0.001)

transport, respectively, in Cu-containing nanoaggregates. It is interesting that the same behavior has been found for the reorganization energies of polythiophene, polyselenophene [46], porphyrin, and porphyrin/C_{60} nanoaggregates [30, 33]. For Ag-containing nanoaggregates, R^2 is only 0.80 and 0.75 for cation polarons and anion polarons, respectively, reflecting the irregular changes in nanoaggregate geometry as the nanoaggregate size is increased. Extrapolated to an infinite nanoaggregate length, the reorganization energies are essentially zero for electron transport in both Cu and Ag nanoaggregates; indeed, the reorganization energy of the 13DOP-Cu− nanoaggregate is zero. The reorganization energies λ_+ and λ_- for hole transport extrapolated to infinite nanoaggregate length are only slightly higher (Table 3). Therefore, all other things being equal, Cu- and Ag-containing nanoarrays should show good charge mobility for both electrons and holes. Cu-containing nanoarrays appear to be the more interesting due to their regular structures and

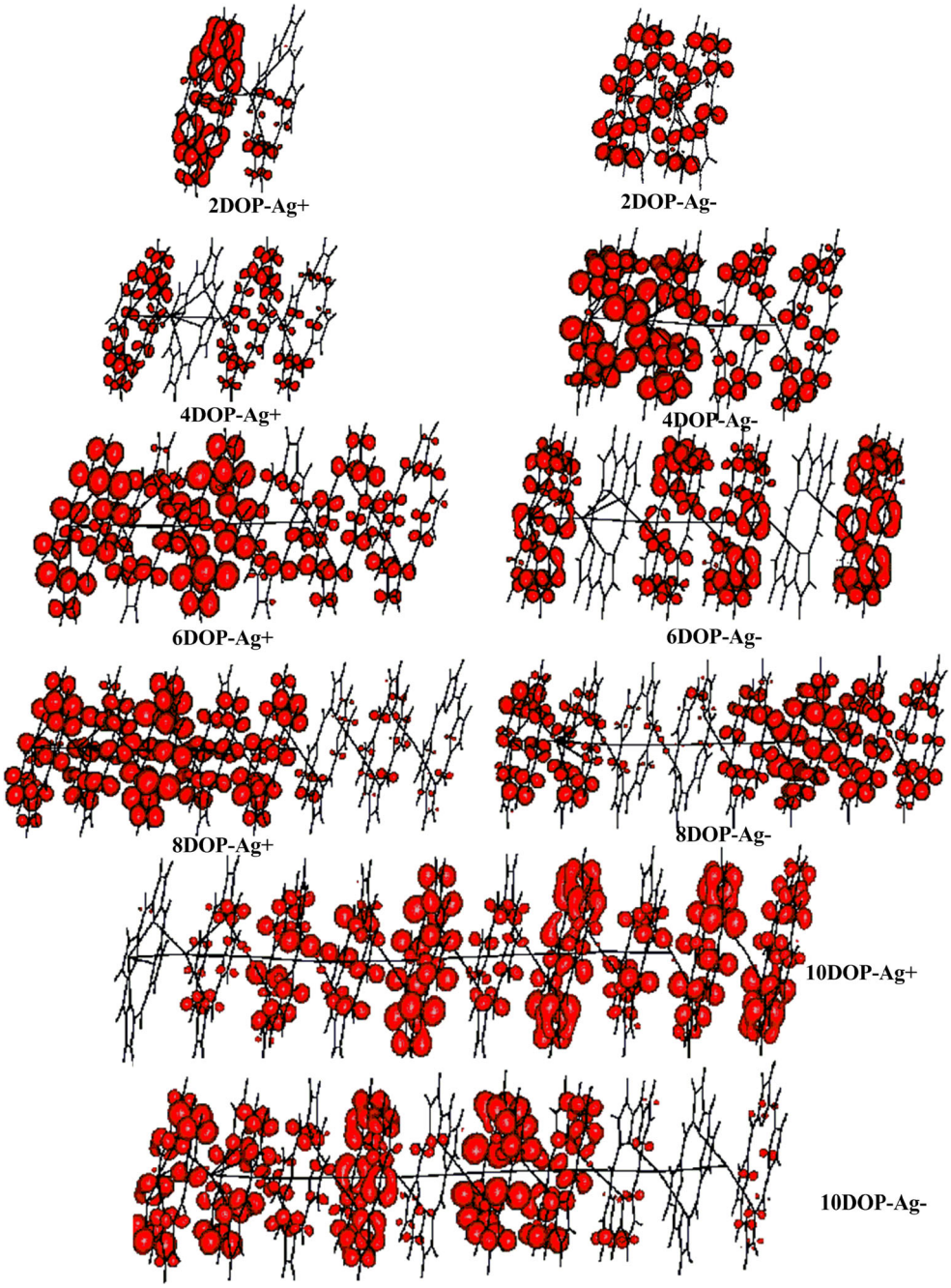

Fig. 5 Unpaired spin-density delocalization in cation and anion radicals of Ag-containing nanoarrays. (Isovalue=0.001)

strong interactions between the Cu atoms and the macrocycles.

Conclusions

21,23-Dioxaporphyrin forms stable complexes with neutral atoms of Zn, Cd, Cu, Ag, and Au, but not with Hg due to its large atomic radius. The formation of these complexes is accompanied by strong charge transfer from the metal to the DOP macrocycle. Nitrogen atoms are mostly responsible for binding to the metal. DOP-M complexes are capable of forming dimers that are largely held together by dispersion forces, unlike their constituent metal complexes, where the contribution of dispersion to the binding energy between the metal atom and the macrocycle does not exceed 30 %. Several types of dimers were found, including face-to-face (F) and various types of parallel-displaced (PD) complexes. F dimers are the lowest-energy dimers for Cu and Ag, while PD dimers are the lowest-energy structures for other systems. Cu- and Ag-containing complexes form stable nanoarrays. According to TD-CAM-B3LYP calculations, the E_g values of

nanoaggregates are <1 eV and decrease slightly as nanoaggregate size increases. No clear correlation between E_g and $1/n$ was observed, with saturation behavior occurring around 0.5 eV. The difference between the atomic radii of Cu and Ag is reflected in the geometries of their nanoaggregates with *n*DOP. In *n*DOP-Cu nanoaggregates, each Cu atom lies in the plane of a macrocycle. On the other hand, in *n*DOP-Ag systems, each Ag atom is positioned between macrocycles. This leads to nanoarrays with alternating Cu–Cu distances for *n*DOP-Cu and irregular Ag–Ag distances for *n*DOP-Ag nanoaggregates. The IP and EA strongly depend upon the number of repeat units due to polaron delocalization over the nanoarray. The IP drops and the EA rises with increasing nanoaggregate size for both Cu- and Ag-containing systems. The polaron delocalization and the related reorganization energies are affected by the identity of the metal present in the system. The reorganization energies are generally small for long nanoaggregates, and are lower for Cu-containing nanoaggregates as they have more extensively delocalized polarons. This is an indicator of good charge mobility in nanoaggregates.

Acknowledgments The authors acknowledge financial support from DGAPA (grant IN100712/25)

References

1. Arai T, Kobata K, Mihara H, Fujimoto T, Nishino N (1995) A membrane protein model: polypeptides with four α-helix bundle structure on 5,10,15,20-tetrakis[2-carboxymethoxy)phenyl]porphyrin. Bull Chem Soc Jpn 68:1989–1998
2. Arai T, Takei K, Nishino N, Fujimoto T (1996) Solvent-dependent chiral assembling of two zinc porphyrins in a zinc–free-base–zinc trimeric porphyrin array. Chem Commun 2133–2134
3. Dailey HA (1990) Biosynthesis of heme and chlorophylls. McGraw-Hill, New York
4. Geier GR, Sasaki T (1997) The design, synthesis and characterization of a porphyrin-peptide conjugate. Tetrahedron Lett 38:3821–3824
5. Rabanal F, Gibney BR, DeGrado WF, Moser CC, Dutton PL (1996) Engineering photosynthesis: synthetic redox proteins. Inorg Chim Acta 243:213–218
6. Crute M (1959) The crystal structure of nickel etioporphyrin II. Acta Crystallogr 12:24–28
7. Iengo E, Zangrando E, Alessio E (2006) Synthetic strategies and structural aspects of metal-mediated multiporphyrin assemblies. Acc Chem Res 39:841–851
8. Imahori H, Umeyama T (2009) Donor−acceptor nanoarchitecture on semiconducting electrodes for solar energy conversion. J Phys Chem C 113:9029–9039
9. Kelley RF, Shin WS, Rybtchinski B, Sinks LE, Wasielewski MR (2007) Photoinitiated charge transport in supramolecular assemblies of a 1,7,*N*,*N*′-tetrakis(zinc porphyrin)-perylene-3,4:9,10-bis(dicarboximide). J Am Chem Soc 129:3173–3181
10. Yoshimoto S, Itaya K (2007) Advances in supramolecularly assembled nanostructures of fullerenes and porphyrins at surfaces. J Porphyrins Phthalocyanines 11:313–333
11. Nakamura Y, Aratani N, Osuka A (2007) Cyclic porphyrin arrays as artificial photosynthetic antenna: synthesis and excitation energy transfer. Chem Soc Rev 36:831–845
12. Guldi DM, Taieb H, Rahman GMA, Tagmatarchis N, Prato M (2005) Novel photoactive single-walled carbon nanotube–porphyrin polymer wraps: efficient and long-lived intracomplex charge separation. Adv Mater 17:871–875
13. Even P, Boitrel B (2006) Crown porphyrins. Coord Chem Rev 250: 519–541
14. Diederich F, Felber B (2002) Supramolecular chemistry of dendrimers with functional cores. Proc Natl Acad Sci USA 99: 4778–4781
15. Meunier B (1992) Metalloporphyrins as versatile catalysts for oxidation reactions and oxidative DNA cleavage. Chem Rev 92:1411–1456
16. Bonifazi D, Accorsi G, Armaroli N, Song FY, Palkar A, Echegoyen L, Scholl M, Seiler P, Jaun B, Diederich F (2005) Oligoporphyrin arrays conjugated to [60]fullerene: preparation, NMR analysis, and photophysical and electrochemical properties. Helv Chim Acta 88: 1839–1884
17. Facci P, Fontana MP, Dalcanale E, Costa M, Sacchelli T (2000) Molecular reorganization in Langmuir−Blodgett films of mesogenic Zn−porphyrin octaesters. Langmuir 16:7726–7730
18. Natale CD, Paolesse R, Macagnano A, Nardis S, Martinelli E, Dalcanale E, Costa M, D'Amico A (2004) Sensitivity–selectivity balance in mass sensors: the case of metalloporphyrins. J Mater Chem 14:1281–1287
19. Mammana A, D'Urso A, Lauceri R, Purrello R (2007) Switching off and on the supramolecular chiral memory in porphyrin assemblies. J Am Chem Soc 129:8062–8063
20. Ahn TK, Kim KS, Kim DY, Noh SB, Aratani N, Ikeda C, Osuka A, Kim D (2006) Relationship between two-photon absorption and the π-conjugation pathway in porphyrin arrays through dihedral angle control. J Am Chem Soc 128:1700–1704
21. Hoeben FJM, Wolffs M, Zhang J, De Feyter S, Leclère P, Schenning APHJ, Meijer EW (2007) Influence of supramolecular organization on energy transfer properties in chiral oligo(*p*-phenylene vinylene) porphyrin assemblies. J Am Chem Soc 129: 9819–9828
22. Kurotobi K, Kim KS, Noh SB, Kim D, Osuka A (2006) A quadruply azulene-fused porphyrin with intense near IR absorption and a large two-photon absorption cross section. Angew Chem Int Ed 45: 3944–3947
23. Kim D, Osuka A (2004) Directly linked porphyrin arrays with tunable excitonic interactions. Acc Chem Res 37:735–745
24. Hwang IW, Kamada T, Ahn TK, Ko DM, Nakamura T, Tsuda A, Osuka A, Kim D (2004) Porphyrin boxes constructed by homochiral self-sorting assembly: optical separation, exciton coupling, and efficient excitation energy migration. J Am Chem Soc 126:16187–16198
25. Aimi J, Oya K, Tsuda A, Aida T (2007) Chiroptical sensing of asymmetric hydrocarbons using a homochiral supramolecular box from a bismetalloporphyrin rotamer. Angew Chem Int Ed 46:2031–2035
26. Tsuda A, Sakamoto S, Yamaguchi K, Aida T (2003) Novel supramolecular multicolor thermometer by self-assembly of a π-extended zinc porphyrin complex. J Am Chem Soc 125:15722–15723
27. Hu JS, Guo YG, Liang HP, Wan LJ (2005) Three-dimensional self-organization of supramolecular self-assembled porphyrin hollow hexagonal nanoprisms. J Am Chem Soc 127:17090–17095
28. Fathalla M, Neuberger A, Li S-C, Schmehl R, Diebold U, Jayawickramarajah J (2010) Straightforward self-assembly of porphyrin nanowires in water: harnessing adamantane/β-cyclodextrin interactions. J Am Chem Soc 132:9966–9967

29. Broadhurst MJ, Grigg R, Johnson AW (1971) Synthesis of porphyrin analogues containing furan and/or thiophen rings. J Chem Soc C 3681–3690
30. Jiménez U, Torres A, Fomine S (2014) Zinc-, cadmium-, and mercury-containing one-dimensional tetraphenylporphyrin arrays: a DFT study. J Mol Model 20:2206–2218
31. Sridevi B, Jeyaprakash Narayanan SJ, Srinivasan A, Chandrashekar TK, Subramanian J (1998) Spectral, magnetic and electrochemical properties of metal oxa- and oxathia-porphyrins. J Chem Soc Dalton Trans 1979–1984
32. Chmielewski PJ, Latos-Grażyński L (1998) Organonickel complexes of 21,23-dioxaporphyrin. Identification of the paramagnetic organonickel(II) complex with two ^{1}-phenyl ligands. Inorg Chem 37:4179–4183
33. Jiménez U, Guadarrama P, Fomine S (2013) Large face to face tetraphenylporphyrin/fullerene nanoaggregates. A DFT study. Org Electron 14:2617–2627
34. Perdew JP, Burke K, Ernzerhof M (1996) Generalized gradient approximation made simple. Phys Rev Lett 77:3865–3868
35. Perdew JP, Burke K, Ernzerhof M (1997) Errata: generalized gradient approximation made simple. Phys Rev Lett 78:1396–1396
36. TURBOMOLE GmbH (2014) TURBOMOLE V6.6. TURBOMOLE GmbH, Karlsruhe. http://www.turbomole.com
37. Grimme S, Antony J, Ehrlich S, Krieg H (2010) A consistent and accurate ab initio parametrization of density functional dispersion correction (DFT-D) for the 94 elements H–Pu. J Chem Phys 132: 154104
38. Jung Y, Head-Gordon M (2006) A fast correlated electronic structure method for computing interaction energies of large van der Waals complexes applied to the fullerene–porphyrin dimer. Phys Chem Chem Phys 8:2831–2840
39. Yang S, Olishevski P, Kertesz M (2004) Bandgap calculations for conjugated polymers. Synth Met 141:171–177
40. Yanai T, Tew DP, Handy NC (2004) A new hybrid exchange–correlation functional using the Coulomb-attenuating method (CAM-B3LYP). Chem Phys Lett 393:51–57
41. Hirata S, Head-Gordon M (1999) Time-dependent density functional theory within the Tamm–Dancoff approximation. Chem Phys Lett 314:291–299
42. Peach MJG, Williamson MJ, Tozer DJ (2007) Influence of triplet instabilities in TDDFT. J Chem Theory Comput 7:3578–358542
43. Lin BC, Cheng CP, Lao ZPM (2003) Reorganization energies in the transports of holes and electrons in organic amines in organic electroluminescence studied by density functional theory. J Phys Chem A 107:5241–5251
44. Malagoli M, Brédas JL (2000) Density functional theory study of the geometric structure and energetics of triphenylamine-based hole-transporting molecules. Chem Phys Lett 327:13–17
45. Sakanoue K, Motoda M, Sugimoto M, Sakaki S (1999) A molecular orbital study on the hole transport property of organic amine compounds. J Phys Chem A 103:5551–5556
46. Zade SS, Bendikov M (2008) Study of hopping transport in long oligothiophenes and oligoselenophenes: dependence of reorganization energy on chain length. Chem Eur J 14:6734–6741